Complex processes in simple ices : laboratory and observational studies of gas-grain interactions during star formation

Öberg, K.I.

12 Cold gas as an ice diagnostic towards low mass protostars

Up to 90% of the chemical reactions during star formation occurs on ice surfaces, probably including the formation of complex organics. Only the most abundant ice species are however observed directly by infrared spectroscopy. This study aims to develop an indirect observational method of ices based on non-thermal ice desorption in the colder part of protostellar envelopes. The IRAM 30m telescope was employed to observe two molecules that can be detected both in the gas and the ice, CH_3OH and HNCO, toward 4 low mass embedded protostars. Their respective gas-phase column densities are determined using rotational diagrams. The relationship between ice and gas phase abundances is subsequently determined. The observed gas and ice abundances span several orders of magnitude. Most of the CH_3OH and HNCO gas along the lines of sight is inferred to be quiescent from the measured line widths and the derived excitation temperatures, and hence not affected by thermal desorption close to the protostar or in outflow shocks. The measured gas to ice ratio of $\sim 10^{-4}$ agrees well with model predictions for non-thermal desorption under cold envelope conditions and there is a tentative correlation between ice and gas phase abundances. This indicates that non-thermal desorption products can serve as a signature of the ice composition. A larger sample is however necessary to provide a conclusive proof of concept.

Published by Öberg K. I., Bottinelli, S. and van Dishoeck, E. F., 2009, A&A, volume 494, pages L13-L16

12.1 Introduction

In cold pre-stellar cores, more than 90% of all molecules, except for H_2, are found in ices (Caselli et al. 1999; Bergin et al. 2002). These ices build up through accretion of atoms and molecules onto cold (sub)micron-sized silicate particles and subsequent hydrogenation to form e.g. H_2O from O (Léger et al. 1985; Boogert & Ehrenfreund 2004). Observations show that H_2O is the main ice constituent in most lines of sight, with a typical abundance of 1×10^{-4} with respect to H_2, followed by CO, CO_2 and CH_3OH (Gibb et al. 2004; Pontoppidan et al. 2004).

During star formation, these ices may be modified by interactions with cosmic rays, UV irradiation, and heating to form complex organic species (Garrod et al. 2008). Gas phase complex species have been observed toward several high and low mass protostars, so-called hot cores and corinos (Bisschop et al. 2007c; Bottinelli et al. 2007). Whether these molecules are formed in the ice and subsequently evaporated, or formed in the hot gas phase from desorbed simpler ices such as CH_3OH is still debated. This is not easily resolved because the abundances of the solid complex molecules are too low to be detected with infrared observations of ices even if they are present in the ice. Therefore, observing gas-phase abundances in the cold envelope may be the most robust constraint on complex ice processes available.

Experimental investigations have concluded that non-thermal desorption is efficient for several common ice molecules, such as CO, CO_2, and H_2O, with photodesorption yields of $\sim 10^{-3}$ per incident photon (Westley et al. 1995a; Öberg et al. 2009b,a). Photodesorption is possible inside cold dark cloud cores and protostellar envelopes because of constant UV fields generated from cosmic ray interactions with H_2 (Shen et al. 2004). Thus a small, but significant, part of the molecules formed in the ice should always be present in the gas phase. This explains observed abundances of gas phase CH_3OH in translucent clouds, dark cloud cores and protostellar envelopes (Turner 1998; Maret et al. 2005; Requena-Torres et al. 2007). The amount of CH_3OH gas observed in these environments suggests that complex molecules (e.g. methyl formate) that form in the ice should be observable in the gas phase due to ice photodesorption, if their abundance ratios with respect to CH_3OH in the ice are the same as observed in hot cores and corinos.

For the first time, we combine infrared ice observations and millimeter gas observations for the same lines of sight to investigate the connection between ice and quiescent gas abundances. We focus on the only commonly observed ice components that have rotational transitions in the millimeter spectral range – CH_3OH and HNCO. The CH_3OH ice abundances in low mass protostellar envelopes vary between 1–30% with respect to H_2O ice (Boogert et al. 2008). It is also one of the most common hot corino gas phase molecules with typical abundances of 10^{-7} – 10^{-6} with respect to H_2. HNCO gas is also commonly detected in hot cores. Solid HNCO (in the form of OCN^-) is only detected toward a few low mass protostars, but strict upper limits exist for more, resulting in an abundance span of an order of magnitude (van Broekhuizen et al. 2005). These large variations in ice abundances imply that CH_3OH and HNCO are appealing test cases for our theory that quiescent complex gas abundances reflect the composition of the co-existing ice mantles, under the assumption that OCN^- is protonated during desorption.

We have observed gas phase CH_3OH and HNCO with the IRAM 30m toward four low mass protostars for which CH_3OH and HNCO ice detections or upper limits already exist. Two of these sources also have OCN^- ice upper limits. These sources are complemented with literature values to constrain further the relationship between ice and gas phase abundances.

12.2 Source selection

Table 12.1 – Targets with pointing positions and ice data.

Source	RA	Dec	V_{LSR} km s^{-1}	α 2–24 μm	cloud
IRAS 03254+3050	03:26:37.45	+30:51:27.9	5.1	0.90	Perseus
B1-b	03:33:20.34	+31:07:21.4	6.5	0.68	Perseus
L1489 IRS	04:04:43.37	+26:18:56.4	7.1	1.10	Taurus
SVS 4-5	18:29:57.59	01:13:00.6	7.8	1.26	Serpens

The four sources IRAS 03254+3050, B1-b, L1489 IRS and SVS 4-5 were chosen from the 'cores to disks' (*c2d*) sample of low mass protostars with ice detections (Boogert et al. 2008) to span CH_3OH abundances of 4 – 25% with respect to H_2O. The *c2d* sample partly overlaps with an earlier ground based survey using the VLT, for which the OCN^- abundances and upper limits were determined (van Broekhuizen et al. 2005) and two of the sources have OCN^- ice upper limits (Table 12.1–12.2).

Table 12.2 – Targets with ice data.

Source	H_2O col. dens. 10^{18}cm^{-2}	CH_3OH % H_2O	HNCO % H_2O
IRAS 03254+3050	3.66	<4.6	–
B1-b	17.67	11.2	–
L1489 IRS	4.26	4.9	<0.06
SVS 4-5	5.65	25.2	<0.27

According to the classification scheme of Lada & Wilking (1984), all sources are embedded class 0/I sources with spectral energy distribution (SED) slopes in the mid-infrared 2–24 μm between 0.68 and 1.26. Their envelopes are of similar mass, as traced by the H_2O ice abundance, with the possible exception of B1-b, which has a factor of 3 higher column density. Except for SVS 4-5 the sources are isolated on the scale of the IRAM 30m beam. Both B1-b and L1489 IRS have however moderate outflows associated with them that may contribute to the detected lines (Jørgensen et al. 2006; Girart et al. 2002).

SVS 4 region is one of the densest nearby star-forming regions and SVS 4-5 is located ~20" away from the class 0 low-mass protostar SMM 4, which has a large envelope and an associated outflow. In addition, the young stellar objects SVS 4-2–12 are all located within 30″ of SVS 4-5 and the emission from SVS 4-5 is probably contaminated by emission from its surroundings when observed with a beam of width as large as 24" (as is the case here). Despite these complications in interpreting the data, SVS 4-5 is included in the sample because of its unusually high CH_3OH ice abundance, which was determined from ice mapping of the SVS 4 region by Pontoppidan et al. (2004).

12.3 Observations

The observations were carried out in March 2008 with the 30-m telescope of the Institut de RadioAstronomie Millimétrique (IRAM). The positions used for pointing are listed in Table 12.1. The line frequencies are taken from the JPL molecular database. Although the observations were centered on the protostars themselves, the choice of low excitation lines and relatively large beams ensures that the cold outer envelope is almost completely sampled. Specifically, we targeted CH_3OH transitions with E_{up}, the energy of the upper level of the transition, between 7 and 100 K. The HNCO lines were observed after the preliminary reduction of the CH_3OH data, and because of its low excitation temperature we chose to observe two of the lowest lying HNCO transitions with E_{up} of 15 and 19 K. The observations were carried out using four different receiver settings with the frequency ranges shown in Table 12.3. Each receiver was connected to a unit of the autocorrelator, with spectral resolutions of 80 or 320 kHz and bandwidths between 80 and 480 MHz, equivalent to a velocity resolution of 0.3, 0.4 and 0.2 km s^{-1} in settings 1, 2, and 3/4, respectively. Typical system temperatures were 100-200 K, 200-500 K, and 700-1000 K, at 3, 2, and 1 mm, respectively.

All observations were carried out using wobbler switching with a 110″ throw in azimuth. Pointing and focus were regularly checked using planets or strong quasars, providing a pointing accuracy of 3″. All intensities reported in this paper are expressed in units of main-beam brightness temperature, which were converted from antenna temperatures using main beam efficiencies of 76, 69, and 50%, at 3, 2, and 1 mm. At these wavelengths, the beam sizes were 24, 16, and 10″, respectively.

12.4 Results

Figure 12.1 shows the spectra derived for setting 1, which is the only setting in which CH_3OH is detected. Figure 12.2 shows the obtained spectra in settings 3 and 4, with all targets observed in both settings except for B1-b. The observed lines were fitted with a single Gaussian to calculate the line widths and integrated intensities in Table 12.3. The Gaussian fits were restricted to exclude the wings observable for B1–b and SVS 4–5. The resulting line widths range from 0.4 to 4.0 km s^{-1}, but three of the sources (B1-b, IRAS 03254, and L1489 IRS) consistently have line widths of below 1 km s^{-1} (Table 12.4).

Table 12.3 – Observed frequencies and targeted molecules at the four different settings.

Frequency (GHz)	Transition[a]	E_u (K)	rms (mK)	Integrated intensity [uncertainty] (K km s^{-1}) IRAS 03254	B1-b	L1489 IRS	SVS 4-5
CH_3OH							
96.739 (E^-)	$2_{12} - 1_{11}$	20.0	11–15	0.11 [0.03]	1.65 [0.22]	0.10 [0.03]	1.47 [0.33]
96.741 (A^+)	$2_{02} - 1_{01}$	14.4		0.16 [0.04]	2.18 [0.21]	0.17 [0.05]	2.72 [0.58]
96.745 (E^+)	$2_{02} - 1_{01}$	27.5		0.017 [0.017]	0.37 [0.20]	0.024 [0.024]	0.64 [0.39]
96.756 (E^+)	$2_{11} - 1_{10}$	35.4		<0.01	0.09 [0.26]	<0.024	0.074 [0.030]
251.738 ($A^\pm$)	$6_{33} - 6_{24}$	98.6	28–40	<0.033	–	<0.079	<0.26
HNCO							
109.906	$5_{05} - 4_{04}$	15.4	15–23	0.038 [0.030]	–	<0.027	0.22 [0.07]
131.886	$6_{06} - 5_{05}$	18.6	19–29	<0.021	0.43 [0.06]	<0.037	0.22 [0.07]

[a] The quantum numbers for the pure rotational transitions of CH_3OH and HNCO are $J_{K_aK_c}$ and $J_{K_{-1}K_{+1}}$, respectively.

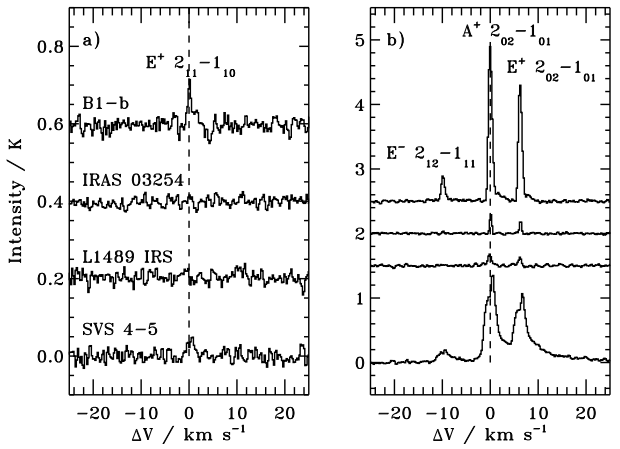

Figure 12.1 *– The observed CH_3OH lines in setting 1 toward the four low mass protostars plotted versus ΔV, the deviation from the source V_{lsr}. The data in the left panel are centered on a rest frequency of 96.756 GHz and in the right panel on a rest frequency of 96.741 GHz.*

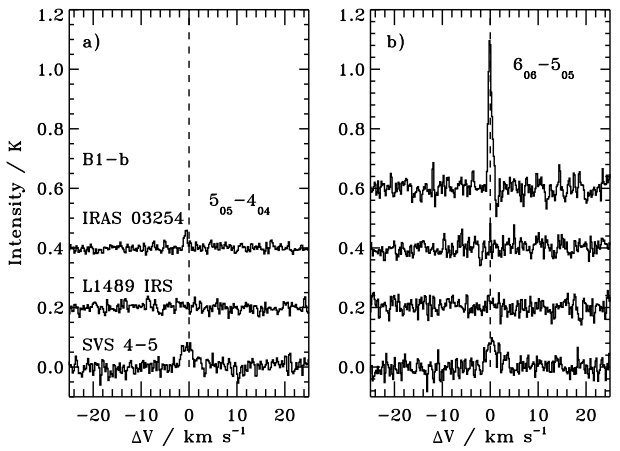

Figure 12.2 *– The observed HNCO lines in setting 3 and 4 plotted versus ΔV, the deviation from the source V_{lsr}. The data in the left panel are centered on a rest frequency of 109.906 GHz and in the right panel on 131.886 GHz.*

Coupled with the low excitation temperatures (below), we most likely probe the quiescent envelope rather than outflows or hot corinos. The fourth source SVS 4–5 has several emission components, reflecting the complexity of the SVS 4 region and containing contributions from non-quiescent gas in for example the nearby outflow from SMM 4. The typical envelope angular size for the source distance is ∼1', which is larger than the largest beam size. Hence, we assume in the analysis that there is no beam dilution.

In Figs. 12.3 and 12.4, we use the rotational diagram method (Goldsmith & Langer 1999) to derive rotational temperatures and column densities. The relations evident in the CH_3OH diagrams are approximately linear, with a possible slight deviation for the one CH_3OH A detection. A line is fitted to all CH_3OH detections, with the assumption that the populations of E and A species are approximately equal. The 2σ upper limits

(derived from the rms in Table 12.3) are overplotted to enable us to ensure that they do not provide further constraints on the fitted line. Except for SVS 4-5, HNCO column densities were derived using the CH_3OH rotational temperatures. The lower limit to the CH_3OH temperature of 4 K was used for IRAS 03254 to accommodate the strict upper limit from setting 3 (Table 12.4). The resulting CH_3OH and HNCO temperatures vary between 4 and 9 K and the CH_3OH and HNCO column densities vary between $1.8 - 27 \times 10^{13}$ and $0.095 - 2.4 \times 10^{13}$ cm^{-2}, respectively. CH_3OH is easily sub-thermally excited at the expected densities in outer protostellar envelopes of approximately 10^4 cm^{-3} and hence the rotational temperature cannot be directly translated into a kinetic temperature (Bachiller et al. 1995).

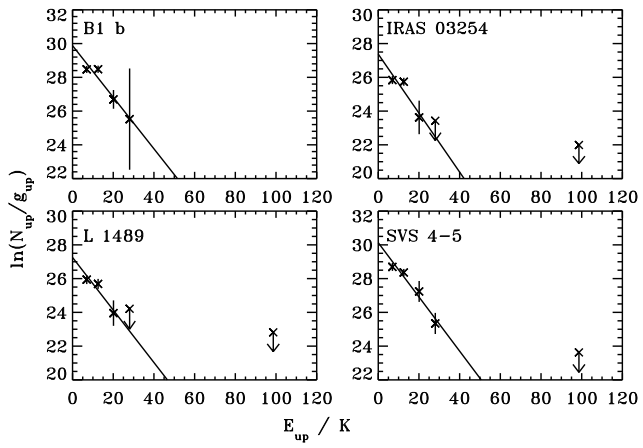

Figure 12.3 *– CH_3OH rotation diagrams including detections and upper limits.*

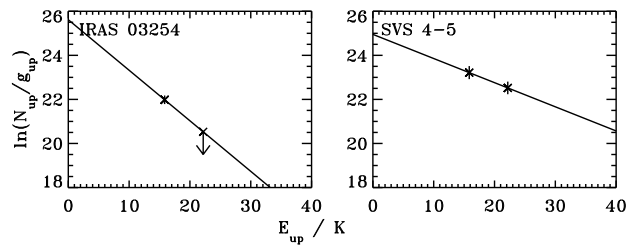

Figure 12.4 *– HNCO rotation diagrams where both lines are detected or the upper limit is strict.*

In previous studies, gas phase CH_3OH was observed toward three other low mass protostars that were also observed by Spitzer to study ices (Boogert et al. 2008): Elias 29, R CrA 7A, and B (Table 12.4). The line widths imply that the observed CH_3OH lines toward Elias 29 trace quiescent material, while those observed toward R CrA 7A and B

Table 12.4 – The calculated temperatures and column densities.

Source	Molecule	Line width (km s^{-1})	T_{rot} (K)	N_X ($\times 10^{13}$ cm^{-2})
IRAS 03254	CH_3OH	0.42–0.49	6±2	1.8±1.8
	HNCO	0.77	~4	~0.48
B1-b	CH_3OH	0.77–0.88	7±1	25±13
	HNCO	0.86	~7	~2.4
L1489 IRS	CH_3OH	0.75-0.97	6±2	1.8±1.3
	HNCO	–	~6	<0.095
SVS 4-5	CH_3OH	2.4–4.0	7±1	27±10
	HNCO	2.6–2.9	9±6	0.38±0.38
Elias 29[a]	CH_3OH	1.3	~ 9	~0.73
R CrA 7A[b]	CH_3OH	2.4–3.0	18±2	59±28
R CrA 7B[b]	CH_3OH	2.1–2.6	19±1	94±28

[a]Buckle & Fuller (2002) [b]derived from Schöier et al. (2006) using rotational diagrams.

do not.

Figure 12.5 shows the correlation between gas and ice abundances of CH_3OH and HNCO, including the literature sources. The abundances are with respect to the H_2O ice column density, which was found to correlate well with the cold dust column density (Whittet et al. 2001). Hence this is a reasonable normalization factor for the lines of sight with quiescent gas, here defined to be line widths $\lesssim$ 1 km s^{-1}, that originates in the cold envelope. It is not a priori a good normalizer for sources with non-quiescent emission, but for consistency the same normalization method is used for all sources. Figure 12.5 illustrates a possible correlation between the gas and ice abundances and upper limits for the quiescent sources – the correlation is not statistically significant due to the many upper limits. The two open triangles in the figure are the RCrA sources, whose higher ratio of gas to ice phase abundance can be attributed to an enhanced radiation field in the region (van Kempen et al. 2008). The measured average gas to solid abundance ratio is 1.2×10^{-4} for the quiescent gas. This probably underestimates the true gas to ice ratio because the absorption and emission observations differ, i.e., the gas phase observations probe on average less dense regions than the ice observations.

12.5 Discussion

Ice photodesorption predicts gas to ice ratios of $10^{-4} - 10^{-3}$ (see Appendix) for typical photodesorption yields and envelope conditions. The measured gas to ice ratio in this study of 1.2×10^{-4} agrees well with this prediction, when accounting for the fact that the measured ratio probably underestimates the true gas to ice ratio. The dashed lines in Fig. 12.5 further show that all quiescent detections and upper limits are consistent with gas to ice ratios of $(1 - 5) \times 10^{-4}$. This agreement and the narrowness of the line widths, supports the interpretation that the emission in these lines of sight originates in the cold,

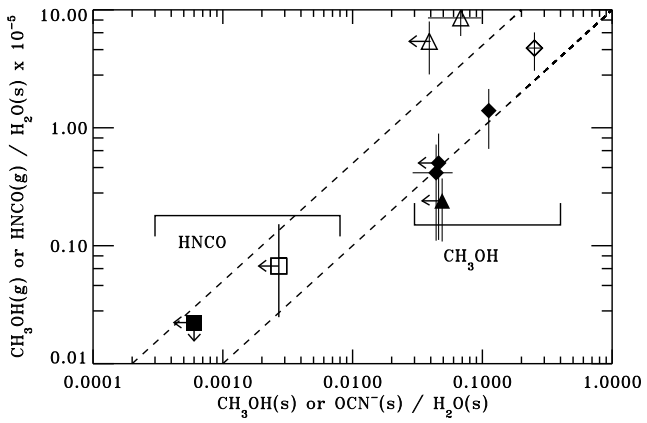

Figure 12.5 *– The correlation between ice and gas phase abundances of CH_3OH (diamonds and triangles) and HNCO (squares). The filled symbols represent quiescent gas (<1.3 km s^{-1}) and the open symbols non-quiescent gas (>2.4 km s^{-1}). In the case of CH_3OH, the diamonds represent measurements from this study and triangles from the literature. The dashed lines show constant CH_3OH(gas)/CH_3OH(solid) or HNCO(gas)/OCN^-(solid) ratios of 1×10^{-4} and 5×10^{-4}.*

quiescent envelope. It also demonstrates that photodesorption alone is sufficient to release the observed ice into the gas, even though other non-thermal processes are not excluded since lack of experimental studies on most non-thermal desorption pathways prevents us from quantifying their relative importance. Gas phase reactions can however be excluded since there is no efficient gas phase reaction pathway to form either CH_3OH or HNCO at the observed abundances (Garrod et al. 2007, Hassel private comm.).

The tentative correlation between gas and ice phase abundances in this pilot study supports the idea that it is possible to determine ice composition by observing the small fraction of the ice that is non-thermally released into the gas phase. To show conclusively that this method works, the size of the sample studied here must be increased and the uncertainty in the derived column densities must be reduced by observing more emission lines. It is also important to remember that until photodesorption data are available for all potential ice species there will be at least a factor of two uncertainty in ice composition estimates using this method due to the different break-up probabilities of different molecules during photodesorption (Öberg et al. 2009b,a). Nonetheless, the method presented here represents a significant improvement on the current lack of observational tools to study complex ices in quiescent regions.

Appendix: Derivation of gas to ice ratios

The gas to ice ratio for a particular species in a protostellar envelope can be estimated by assuming a steady-state between photodesorption and freeze-out:

$$Y_{\rm pd} \times I_{\rm UV} \times \sigma_{\rm gr} \times f_{\rm x} = 4.57 \times 10^4 \times \left(\frac{T}{m_{\rm x}}\right)^{\frac{1}{2}} \times \sigma_{\rm gr} \times n_{\rm x}^{g} \tag{12.1}$$

$$f_{\rm x} = \frac{n_{\rm x}^{\rm i}}{n^{\rm i}} \tag{12.2}$$

where $Y_{\rm pd}$ is the photodesorption yield set to be $(1-3)\times10^{-3}$ photon^{-1} from our experiments, $I_{\rm UV}$ is the cosmic-ray-induced UV field of 10^4 photons cm^{-2} s^{-1} and $\sigma_{\rm gr}$ is the grain cross section. The cosmic-ray-induced UV flux assumes a cosmic ray ionization rate of 1.3×10^{-17} s^{-1}. Because photodesorption is a surface process, the photodesorption rate of species x depends on the fractional ice abundance $f_{\rm x}$, which is defined to be the ratio of the number density of species x in the ice, $n_{\rm x}^{\rm i}$, to the total ice number density, $n^{\rm i}$. The freeze-out rate of species x depends on the gas temperature T, which is set to 15 K, the molecular weight $m_{\rm x}$, and the gas number density $n_{\rm x}^{\rm g}$. For an average molecular weight of 32, this results in a gas phase abundance $n_{\rm x}^{\rm g}/n_{\rm H}$ of $(3-9)\times10^{-4} f_{\rm x}/n_{\rm H}$. From this and an average total ice abundance $n^{\rm i}/n_{\rm H}$ of 10^{-4}, the predicted gas to ice phase abundance ratio is:

$$\frac{n_{\rm x}^{\rm g}}{n_{\rm x}^{\rm i}} \sim \frac{(3-9)\times10^{-4}/n_{\rm H}\times f_{\rm x}}{n^{\rm i}/n_{\rm H}\times f_{\rm x}} \sim (3-9)/n_{\rm H} \tag{12.3}$$

For a typical envelope density of 10^4 cm^{-3}, ice photodesorption hence predicts a gas to ice ratio of $10^{-4} - 10^{-3}$. The derivation of a gas to ice ratio from observed cold gas emission lines and ice absorption features in the same line of sight is complicated by the fact that different regions can contribute by varying amounts. The emission features trace gas in the envelope and cloud both in front and behind the protostar, while the ice absorption features only trace envelope material directly in front of the protostar. The column is hence twice as long for the gas observations. This is probably more than compensated for by using beam averaged gas column densities, as is done in this study, because the large beam traces on average less dense material compared to the pencil beam of the ice absorption observations. Note also that the CH_3OH ice abundance may vary between lower and higher density regions. To quantify a conversion factor between the observed and true gas to ice ratio requires detailed modeling of each source which is outside the scope of this study. Instead we here assume that the observed ratio is a lower limit to the true ratio.